A Self-healing Electrical Impedance Tomography Sensor for the Selective Localization of Compression and Damage Based on a Diels-Alder Conductive Composite

Huaijin Chen*, Zhanwei Wang*, Fatemeh Sahraeeazartamar, Seyedreza Kashef Tabrizian, Kevin Langlois, Seppe Terryn, Bram Vanderborght (*same contribution)

***Abstract*—Electrical Impedance Tomography (EIT) tactile sensors are suitable for pressure and tactile sensing on large-scale surfaces due to their simple structure and their capability of spatial continuous measurement. However, their conductive sensing layer is often composed of flexible materials, such as polymers or fabrics, making them susceptible to damage from sharp objects. To address this issue, in this paper, we propose a novel self-healing EIT tactile sensor. Its flexible conductive layer is made from a self-healing polymer, which can restore itself through the Diels-Alder reversible reaction. We achieve a truly selective distinction between pressure and damage areas by using the sandwich structure in sensor design. By adopting the Artificial Intelligence (AI)-enhanced "two-step" imaging method, the experimental result shows an average positioning error of 1.84 mm in the compressed area over a square sensor with an edge length of 100 mm. In the single compressed area cases, the imaging results of the average Image Correlation Coefficient (ICC), Relative Image Error (RIE), and Structural Similarity (SSIM) are 0.80, 0.59, and 0.92, and those of two and three compressed areas are 0.78, 0.66, and 0.78, respectively. Meanwhile, the undamaged section is still functional for tactile sensing when the sensor is partially damaged. Furthermore, after in-situ self-healing and a simple process of updating the baseline voltage, the damaged area fully restores its original functionality.**

***Index Terms*—Electrical Impedance Tomography (EIT), Diels-Alder reaction, self-healing materials, tactile sensor, damage localization**

This work is supported in part by the China Scholarship Council (CSC) under NO. 202106830032; the Wetenschappelijk Onderzoek (FWO) under grant 1258523N, 1274125N, and Vrije Universiteit Brussel (VUB) research council postdoctoral grant OZR4307 (Corresponding author: Huaijin Chen).

H. Chen, Z. Wang, K. Langlois, S. Terryn, S. Tabrizian, and B. Vanderborght are with Brubotics, Vrije Universiteit Brussel and imec, Pleinlaan 2, 1050 Brussels, Belgium (e-mail: Chen.Huaijin@vub.be; Zhanwei.Wang@vub.be; Kevin.Langlois@vub.be; Seppe.Terryn@vub.be; Seyedreza.Kashef.Tabrizian@vub.be; Bram.Vanderborght@vub.be).

F. Sahraeeazartamar and S. Terryn are also with Physical Chemistry and Polymer Science (FYSC), Vrije Universiteit Brussel, Pleinlaan 2, 1050 Brussels, Belgium (e-mail: Fatemeh.Sahraeeazartamar@vub.be).

I. INTRODUCTION

With the growing demand for large-area sensing with minimal wiring, Electrical Impedance Tomography (EIT) is gaining increasing attention for electronic skins [1]. Compared to the other pressure sensors that are composed of discrete sensing units (such as Force Sensitive Resistors array, FSRs array), it has features of simple structure of only limited electrodes mounted on the boundary of the sensor, achieving spatial continuous measurement. Hence, EIT robotic skin is suitable for pressure and tactile sensing on large-scale surfaces [2].

In recent years, various types of EIT sensors have been reported, with fabrication materials including but not limited to conductive elastomers [3, 4], conductive fabric [5], and hydrogels [6, 7]. To improve functionalities, multimodal and stiffness variable EIT sensors are also proposed [8-10]. Several multilayer structure EIT sensors have also been proposed. These can be categorized into those that utilize local equivalent impedance changes under pressure [11] and those that actively inject current into one of the layers, referred to as a "drive layer" [12]. In addition, various EIT sensors with distinct characteristics have been developed, such as high accuracy and highly flexible sensors [13, 14].

In terms of applications, EIT sensors have been utilized in a wide range of fields, such as social touch emotions interpretation [15, 16], robotic arm control [4, 17], tactile sensing for humanoid robots [18], and force monitoring in human-machine interaction for wearable robots [19].

However, one significant challenge for tactile robotic skin is ensuring durability. In most designs, the sensing components are fabricated with flexible materials, which directly interact with the environment through contact and compression. Consequently, due to its softness, robotic skin is prone to failures from damage like cuts and punctures. To address this issue, bioinspired self-healing sensors are proposed. Such self-healing soft sensors, which have been extensively studied in literature [20, 21], can restore both their mechanical and sensing performance after damage. As such they can withstand multiple damage-healing cycles, which extend their lifespan and reduce the need for replacement of any of their

components. Moreover, because these self-healing sensors can withstand multiple damage-healing cycles, they have been investigated for damage detection and localization as well [22]. Whereas many self-healing piezoresistive sensors have been studied in literature, research on self-healing EIT sensors is far more limited. Only hydrogel-based EIT robotic skins were reported for self-healing and damage detection [8, 23]. However, when considering integration into robotics applications, hydrogels exhibit relatively weak stability and low resistance to external environmental changes, particularly in temperature and humidity.

Beyond enhancing the robustness and lifespan of EIT sensors, incorporating self-healing materials in their construction also enables damage localization. Similar to pressure and touch, damage to the conductive sheet alters local conductivity, which can be detected through EIT. However, distinguishing between touch and damage remains a significant challenge, yet it is essential for developing a truly selective multifunctional sensor capable of accurately identifying both.

We propose a novel self-healing EIT sensor made from a self-healing composite, where the matrix consists of a Diels-Alder (DA) crosslinked network filled with Carbon Black (CB) particles to provide conductivity [24-26]. Its reversible Diels-Alder crosslinks enable self-healing, allowing the restoration of significant macroscopic damage while also ensuring mechanical strength and stability. Therefore, this sensor has features of in-situ self-healing functionalities, which are convenient for maintenance. Meanwhile, based on the multilayer structure (also referred to as "sandwich structure") in sensor design [11], this paper introduces a new feature for the EIT sensor. This feature causes the sensor to exhibit completely opposite trends in conductivity under compression and damage, which allows for clear differentiation between damaged and compressed areas, making the sensor truly selective without requiring any complicated algorithms.

The structure of this paper is as follows: In section 2, the EIT methodology is illustrated, and a "two-step" Artificial Intelligence (AI) enhanced method [27, 28] for reconstructing EIT images is presented. Section 3 presents the design of the self-healing EIT sensor and explains the mechanisms of tactile and damage detection. Section 4 provides experimental validation of tactile measurement performance, damage detection capability, and self-healing properties. Finally, conclusions are drawn in section 5.

II. EIT Methodology

The time differential EIT is adopted [29], and it reconstructs the perturbation of the conductivity distribution inside a given domain Ω, as shown in Fig. 1. The stimulation current I is injected through the border of Ω to form an electrical field. When the local conductivity varies (which can be positive or negative), as Ω^+ shown in Fig. 1, the boundary voltage V varies accordingly and is acquired for reconstructing the image. The $\Delta V = V_1 - V_0$ is obtained to reconstruct the conductivity variation, where V_0 is the boundary voltage before the conductivity varies, and V_1 is that after the conductivity varies. The conductivity varying area is referred to as the target area in this study, and the remaining conductivity area (Ω^- in Fig. 1) is referred to as the background.

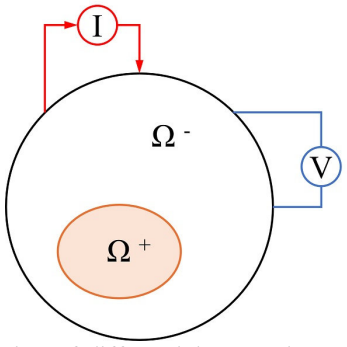

Fig. 1. Illustration of differential EIT, where Ω is the sensing domain, Ω^+ is the conductivity varies area, referred to as target area, and Ω^- of conductivity remains area is referred as background. Stimulation current I is injected to form an electrical field, and boundary voltages V are measured for reconstructing its images.

Using the Finite Element Method (FEM), the EIT problem is expressed as:

$$\Delta \boldsymbol{V} \approx -\int_{pixel\ k} \nabla \boldsymbol{u}(I_i) \cdot \Delta\sigma \cdot \nabla \boldsymbol{u}(I_j) dV \tag{1}$$

where $\Delta\sigma$ is the conductivity perturbation of one pixel in Ω, $\Delta \boldsymbol{V} \in \mathbb{R}^{M\times 1} (M \ll N)$ is its corresponding boundary voltage variation vector, $\nabla \boldsymbol{u}(I_i)$ and $\nabla \boldsymbol{u}(I_j)$ are gradients of the potential fields u when the current is injected into the i^{th} and j^{th} electrodes pairs, respectively [30]. Then, the equation (1) is expressed as:

$$\Delta \boldsymbol{V} \approx J\, \Delta \boldsymbol{\sigma} \tag{2}$$

$$J = -\int_{pixel\ k} \nabla \boldsymbol{u}(I_i) \cdot \nabla \boldsymbol{u}(I_j) dV \tag{3}$$

where $J \in \mathbb{R}^{M\times N}$ is the Jacobian matrix.

The EIT inverse problem is ill-posed and ill-conditioned, so obtaining stable images of high quality is challenging. Recently, AI-based EIT imaging algorithms have shown great promise. One approach, known as "end-to-end" imaging, directly employs AI to reconstruct images from raw voltage data [31]. Another is the "two-step imaging method", where an initial image is first reconstructed using a conventional regularization algorithm and then enhanced by an AI model [27, 28]. The two-step methods demonstrate strong robustness to noise [32], which is a critical feature for EIT pressure sensors that may operate in complex environments.

The two-step imaging method is also adopted in this study. Firstly, to obtain the initial image, the Tikhonov regularization is adopted [33], where the reconstructed conductivity variation of $\Delta\hat{\boldsymbol{\sigma}}$ can be estimated as:

$$\Delta\hat{\boldsymbol{\sigma}} = (J^{\mathrm{T}}J + \lambda L)^{-1} J^{\mathrm{T}} \Delta \boldsymbol{V} \tag{4}$$

where λ is the regularization parameter, and L is the regularization matrix. The non-iteration form of the standard

Tikhonov regularization is adopted, and the identity matrix I is used as matrix L.

Then, an AI model based on the U-Net architecture [34] was built in PyTorch 2.0 and used to enhance the imaging results, as shown in Fig. 2. The network consists of several convolutional blocks, each containing a 3×3 convolutional layer, a Batch Normalization (BN) layer, and a Softsign activation function. The Softsign function was chosen because it is symmetric about the origin, and the conductivity variations in this study include both positive and negative values, corresponding to the compressed regions and damaged regions, respectively. Max pooling with a stride of two was used for down sampling, while nearest neighbor interpolation was applied for up sampling. The U-Net architecture features shortcut connections between the encoder and decoder stages (represented by gray arrows in the figure). In this study, the shortcut connections in U-Net were implemented using channel-wise and pixel-aligned concatenation. Finally, the Softmax function and cross-entropy loss were employed to classify each pixel in the image into three categories, including compressed region, background, and damaged areas.

In total, 14000 data were acquired in simulation, and 12000 data were used as training data and equally split into four categories (each category contains 3000 data). The first three categories contain one, two, and three positive conductivity varying areas respectively, to simulate the compressed areas. The last category contains at least one negative conductivity varying area for damage detection. The other 2000 groups were used as testing data, which share the same data category ratio. In the training process, no specific customized training strategy was used, and no artificial noise was added to the dataset. The Adaptive Moment Estimation (ADAM) was selected as the solver, with a constant learning rate $lr = 1e^{-3}$. The training is performed for 200 epochs with a minibatch size of 64.

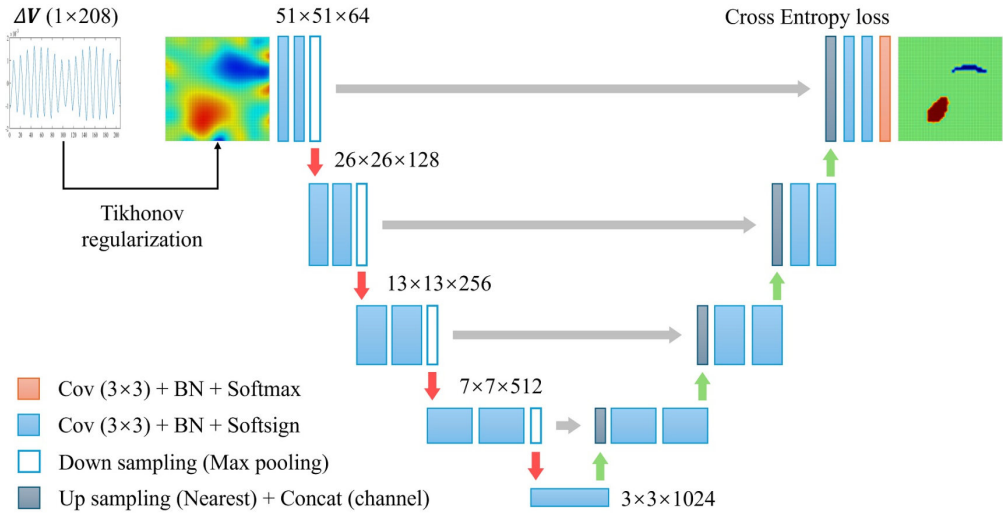

Fig. 2. Two-step imaging methods. The Tikhonov regularization is used to obtain an initial image in the first step. In the second step, a U-Net is used to enhance the image. The cross-entropy loss was employed to classify each pixel in the image into three categories, including compressed region, background, and damaged areas.

III. Sensor Development

In this section, the DA reaction-based self-healing composite is introduced, and the structure of the proposed sensor is presented. The mechanisms of tactile measurement and damage detection are illustrated as well.

A. Self-healing conductive composite synthesis

Intrinsic self-healing materials are favored in this study due to their ability to restore functionality without relying on external healing agents that are embedded in the microcapsules or vascular networks used in extrinsic self-healing systems. For this reason, a DA based polymer is selected for its reversible bonding mechanism and superior resistance to environmental conditions when compared to other intrinsic self-healing materials like hydrogels [35]. Furthermore, to impart electrical conductivity to the composite, Carbon Black (CB) is incorporated into the DA matrix, resulting in a conductive self-healing material suitable for sensing applications.

Referring to our previous work [24-26], the synthesis of the conductive self-healing composite involved an initial reaction between furfuryl glycidyl ether (FGE) and Jeffamine ED2003 via an irreversible epoxy-amine reaction under stoichiometric conditions. The resulting furan-functionalized Jeffamine FED2300 was then dissolved in chloroform and combined with the bismaleimide crosslinker (DPBM) at a maleimide-to-furan ratio of 0.6. To prevent side reactions, hydroquinone (5 wt. % of DPBM) was added as a radical inhibitor. CB Ensaco 360G particles were dispersed in the solution using a Heidolph RZR 2021 mechanical stirrer. The final composite was obtained via solvent casting, with chloroform removed under vacuum at room temperature for 24 hours. The composite

contains CB at 8 wt. %. All chemicals were used as received: FGE (Sage Chemicals), Jeffamine ED2003 (MW 2024 g/mol, Huntsman), DPBM and hydroquinone (Sigma-Aldrich), chloroform (Biosolve Chimie), and carbon black Ensaco 360G (surface area 780 m²/g, IMERYS). B. Sensor structure and mechanism

The sandwich structure is adopted in the sensor design [11], where a lower conductive layer is used as a sensing layer, and electrodes are mounted on it. A higher conductive layer (copper) is used as a shortcut layer. The sensing layer is the most vulnerable part of the sensor, as it is typically made of flexible materials and is in direct contact with the external environment. Therefore, this layer is prioritized in self-healing. In contrast, the shortcut layer, although it serves as part of the sensor, is the outer shell of the robot to support and protect the inner structure of the robot, which is rigid and resistant to damage (composed of hard plastic and metal).

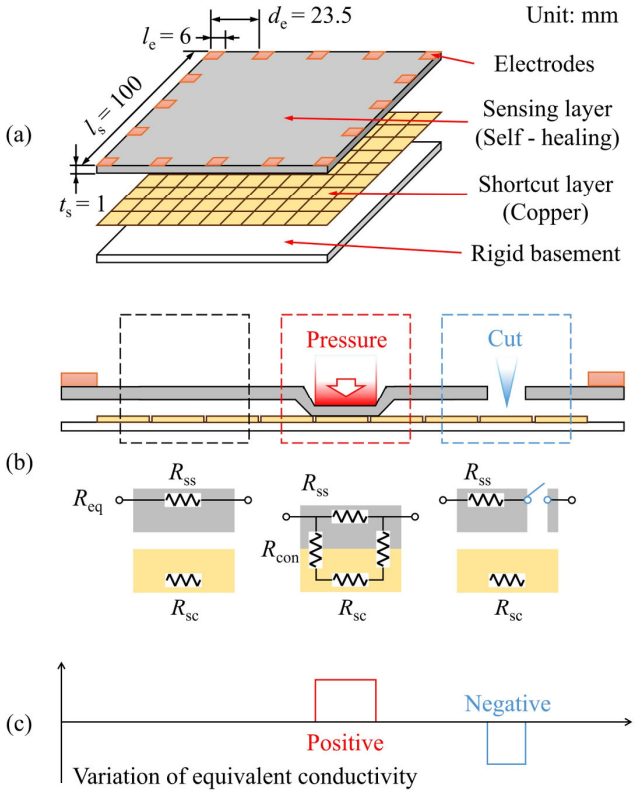

Fig. 3. (a), the sandwich structure is adopted in the proposed sensor. A sensing layer with low conductivity, composed of the conductive self-healing composite, and a shortcut layer with high conductivity, made from copper. In (b), circuit elements are used to illustrate the behaviors of the sensor under various states. (c), the local equivalent conductivity of the sensor increases when compressed and decreases upon damage.

The geometry of the sensor is shown in Fig. 3 (a). The length of the self-healing composite sensing layer is $l_s = 100\,\text{mm}$, and the thickness is $t_s = 1\,\text{mm}$. The size is primarily defined by the fabrication process, particularly the mold used during pressure molding. While the current dimensions are sufficient for validating the proposed self-healing sensor design, they can be further optimized based on the requirements of specific application scenarios. In this study, a typical EIT configuration is employed, with 16 electrodes evenly distributed along the sensor boundary. The electrodes are squares of edge length $l_e = 6\,\text{mm}$, and the distance between electrodes is $d_e = 23.5\,\text{mm}$. The geometry of the sensor is shown in Fig. 3 (a). The length of the self-healing composite sensing layer is $l_s = 100\,\text{mm}$, and the thickness is $t_s = 1\,\text{mm}$. The pseudo-polar current injection and pseudo-polar voltage measurement (pp-pp) protocol is adopted [36, 37].

The basic function of the tactile sensing mechanism is illustrated in Fig. 3 (b), where R_{eq} is the local equivalent resistance, R_{ss} is the resistance of the sensing layer, R_{sc} is the resistance of the shortcut layer, and $R_{ss} \gg R_{sc}$, and R_{con} is the contact resistance between two layers. As the electrodes are arranged on the sensing layer, the stimulation current passes solely through R_{ss} When no external stimuli, resulting in an equivalent resistance of $R_{eq} = R_{ss}$. When the two layers are forced to contact each other as a result of compression, the current can partially flow through the R_{con} and R_{sc} forming parallel to R_{ss} [11]. As a result, the R_{eq} measured in the compressed areas of the sensing layer decreases. Furthermore, the sensing layer in this study is made of a self-healing composite. When the sensing layer is damaged, the local conductivity decreases, and in cases of severe damage, it may become completely non-conductive. Fig. 3 (c) intuitively illustrates the variation in equivalent conductivity, as it changes positively under compression, and negatively when damaged. Due to this design, this novel self-healing EIT sensor is easy to distinguish between compression and damage by analyzing the variations in conductivity.

C. Data acquisition device

A data acquisition device was developed based on the Red Pitaya 125-14 oscilloscope, based on our previous works [9, 19]. The photo and the diagram of the device are shown in Fig. 4 (a) and (b), respectively. A voltage signal is first generated by the Digital-to-Analog Converter (DAC) of the Red Pitaya 125-14 oscilloscope, then converted to the current signal by an enhanced Howland type Voltage Controlled Current Source (VCCS) [38]. The frequency and the amplitude of the current signal are $f = 954\,\text{Hz}$ and $I_{amp} = 0.35\,\text{mA}$, respectively. A multiplexer that is based on ADG1606 chips (a kind of 16-channel analog multiplexer chip) was developed to connect 16 electrodes of the sensor and the data acquisition circuit, which is composed of an Analog-to-Digital Converter (ADC) and an amplifier circuit. The gating of the multiplexer is controlled by the General-Purpose Input Output (GPIO). After the voltage data is acquired from the sensor, the Red Pitaya 125-14 oscilloscope transferred the data to the Personal Computer (PC) with TCP/IP protocol for tomography.

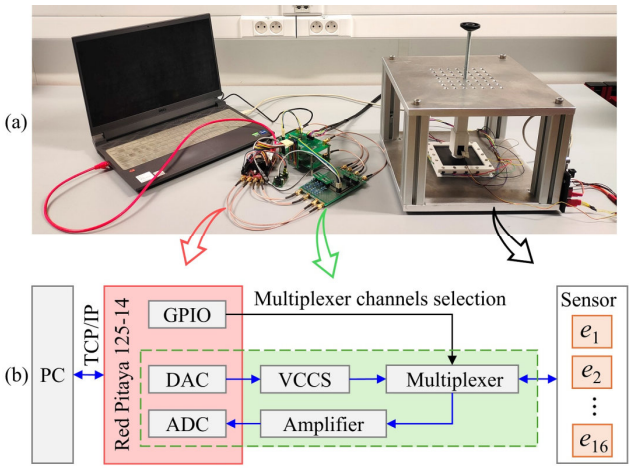

Fig. 4. (a) and (b) are the photo and diagram of the EIT data acquisition device. It is mainly composed of a Red Pitaya 125-14 oscilloscope, a VCCS module, a multiplexer module, and an amplifier circuit.

IV. Experiments

Three objectives were set for experimental validation. Firstly, the electrical self-healing performance of the composite is validated. Secondly, the functionalities of the developed sensor in tactile sensing, also after healed damages. Finally, the performance of the sensor in damage detection and self-healing.

A. Self-healing property of the composite

Firstly, the self-healing performance of the composite is validated. Two samples with the same size of 100 × 10 × 1 mm (length × width × thickness) were fabricated, as shown in Fig. 5. As a control, sample 1 remained intact, while sample 2 was deliberately cut. Both samples then underwent the same self-healing procedure. This design allows us not only to evaluate the intrinsic self-healing capability of the composite, but also to investigate the potential impact of the heating process on its electrical properties.

Fig. 5 (a) illustrates the experimental procedure. In (1), both samples are shown prior to treatment. In (2), sample 2 is cut into two sections. In (3) and (4), after realigning the fractured surfaces, a heat pad is placed on top of both samples. A silicone rubber pad is applied above the heat pad to exert pressure, ensuring better contact and improved heat retention. The self-healing process is carried out at 90 °C for 2 hours, followed by cooling to room temperature. In (5), it is shown that after healing, the damage on sample 2 retains only a faint scar.

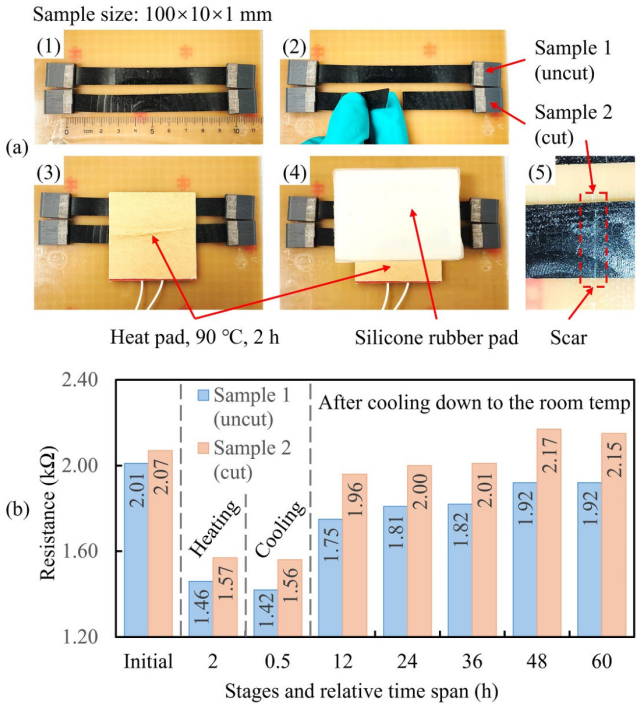

Fig. 5. Two samples were prepared for comparison, where sample 1 remained intact and sample 2 was cut. (a) shows the experimental procedure, where (1) displays the samples before the self-healing test. (2) shows sample 2 being cut into two sections. (3) and (4), with a heat pad and a temperature-maintaining silicone rubber pad, both samples were conducting the procedure of self-healing at a temperature of 90 °C for 2 hours. (5) shows the faint scar on sample 2 after healing. (b) presents the effect of the self-healing process on electrical conductivity. As shown, sample 2 regained conductive capability after healing. In addition, the comparison between the two samples shows that heating causes a temporary increase in conductivity, followed by a gradual recovery toward the original value.

Fig. 5 (b) presents the evolution of electrical conductivity in the samples, which can be divided into four stages. The initial stage represents the original conductivity of the samples, with resistances of 2.01 kΩ and 2.07 kΩ for sample 1 and sample 2, respectively. In the second stage, after the 2-hour heating period for self-healing, sample 2 regains conductive capability, indicating successful healing. Meanwhile, both samples exhibit significantly reduced resistance compared to the initial values, suggesting that heating enhances the conductivity of the composite.

The third stage involves a 0.5-hour cooling period, during which the samples gradually return to room temperature. In the fourth stage, the conductivities of both samples slowly decrease over time, trending back toward their initial values. After 48 hours, the conductivities tend to be stabilized. At this stage, sample 1 has not completely recovered to its initial resistance of 2.01 kΩ, exhibiting instead a slightly reduced value of 1.92 kΩ. However, sample 2 retains a higher

resistance of 2.15 kΩ compared to its initial value of 2.07 kΩ. This slight increase in resistance of sample 2 can be attributed to a small misalignment of the fracture surfaces at the microscopic level, resulting in insufficient reconnection. The conductivity self-healing property is prioritized in this study, and for more detailed discussions on this material, such as its mechanical self-healing capabilities, can be found in our previous work [25].

B. Signal-to-Noise Ratio of the sensor

We evaluated the system-level Signal-to-Noise Ratio (SNR) of the integrated sensor and data acquisition device using the method in references [39, 40]:

$$\mathrm{SNR} = 10 \log \frac{\sum_{n=1}^{N}[V(n)]^2}{\sum_{n=1}^{N}[V(n)-V_{\mathrm{mean}}]^2} \quad (5)$$

where $V(n)$ denotes the voltage data acquired in the n^{th} measurement, and V_{mean} represents the mean value calculated over $N = 500$ repeated measurements under no applied pressure to the sensor. The SNR was computed according to equation (5). Under the 16-electrode pp-pp protocol used in this study, a measurement generates 208 voltage values, referred to as 208 "channels", for each image. The result is shown in Fig.6.

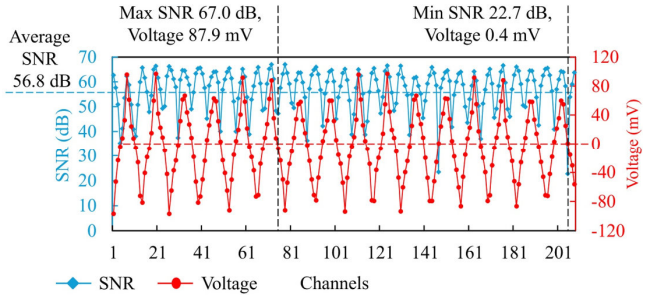

Fig. 6. The primary y-axis (blue line with diamond markers) shows the SNR values for all 208 channels, while the secondary y-axis (red line with circular markers) displays the corresponding measured voltage amplitudes for each channel. As shown, channels with higher voltage amplitudes generally correspond to higher SNRs. The average SNR is 56.8 dB, with a maximum of 67.0 dB and a minimum of 22.7 dB.

In Fig.6, the SNR of all channels is plotted with a blue line with diamond markers along the primary y-axis, while the corresponding measured voltage amplitudes are shown with a red line with circular markers along the secondary y-axis. As shown, the channels with higher voltage amplitudes generally have higher SNR. The average SNR across all channels is 56.8 dB, with the maximum reaching 67.0 dB at 87.9 mV and the minimum at 22.7 dB when the voltage is only 0.4 mV. This trend aligns with the observations of Yang et al. [41], despite differences in stimulation and measurement protocols. One thing to be noted is that although the baseline voltage of some channels is low, this does not imply that they lack useful information, as EIT measures changes in boundary voltages caused by internal conductivity variations. Even with a low baseline voltage, a channel still may respond strongly to specific local conductivity changes, depending on the sensitivity distribution. On the other hand, the imaging method used in this study belongs to the category of two-step imaging methods, which are generally robust to noise [9, 42], supporting the acceptability of the results.

C. Tactile measurement tests

A test platform is used in this test, as shown in Fig. 7. It is composed of a frame and modularized indenters. The indenter can be mounted in different positions on the frame, and the size of the indenter head can be changed according to requirements. Each indenter has an independent load cell (type: FX293X-040B-0100-L) to record the pressure applied to the sensor as validation. More details of the experimental setup can be found in previous work [9].

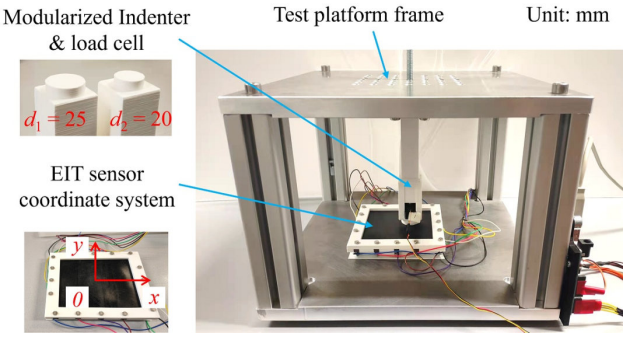

Fig. 7. The experimental platform. The origin of the sensor coordination is positioned at the centroid of the sensor, and the x-axis and y-axis are parallel to the edges of the sensor. Each indenter has an independent loadcell to monitor the pressure.

In this study, two differently sized round indenters with diameters of $d_1 = 25$ mm and $d_2 = 20$ mm were used to apply pressure to the sensor. The sensitivity of the EIT sensor is not evenly distributed, even though the edge area can detect smaller pressure, the same pressure of 80 kPa is used in experiments to control variances. The origin of the sensor coordination is positioned at the centroid of the sensor, and the x-axis and y-axis are parallel to the edges of the sensor. In total, three representative positions of (0, 0), (0, 25), and (25, 25) are selected for this test.

Image Correlation Coefficient (ICC), Relative Image Error (RIE) and structural similarity (SSIM) [43-45] were used as main criteria, which are widely used in EIT studies:

$$\mathrm{ICC} = \frac{(\sigma_{\mathrm{gt}}-\bar{\sigma}_{\mathrm{gt}})\cdot(\sigma_{\mathrm{img}}-\bar{\sigma}_{\mathrm{img}})}{\sqrt{|\sigma_{\mathrm{gt}}-\bar{\sigma}_{\mathrm{gt}}|^2 \cdot |\sigma_{\mathrm{img}}-\bar{\sigma}_{\mathrm{img}}|^2}} \quad (6)$$

$$\mathrm{RIE} = \frac{\|\sigma_{\mathrm{img}}-\sigma_{\mathrm{gt}}\|}{\|\sigma_{\mathrm{gt}}\|} \quad (7)$$

$$\mathrm{SSIM} = \frac{(2\mu_{\mathrm{img}}\mu_{\mathrm{gt}}+C_1)(2\delta_{\mathrm{img,gt}}+C_2)}{(\mu_{\mathrm{img}}^2+\mu_{\mathrm{gt}}^2+C_1)(\delta_{\mathrm{img}}^2+\delta_{\mathrm{gt}}^2+C_2)} \quad (8)$$

where σ_{gt} is the ground truth of conductivity, and σ_{img} is the reconstructed conductivity image. In the equation (8) of SSIM, μ_{img} and μ_{gt} are the local means of the corresponding pixel in

the image and ground truth respectively. δ_{img} and δ_{gt} are their standard deviations. $\delta_{\mathrm{img,gt}}$ is the cross covariance, and C_n are constant used to stabilize the division with weak denominators. More details of SSIM can be seen in [44]. The closer the SSIM and ICC are to 1, the higher the similarity between the reconstructed image and the ground truth. The closer the RIE to 0, the less error between the reconstructed image to ground truth.

The experiment results are shown in Fig. 8, where (a) is the ground truth generated in simulations according to the experimental setups, set as references. P_{gt} is the centroid of the target ground truth. Fig. 8. (b) and (c) are the imaging results of Tikhonov regularization and enhanced images using U-Net. In cases 1-3, the 20 mm indenter was used, while in cases 4-6, the 25 mm indenter was used. The test results in Fig. 8 (b) indicate that the compressed areas in all the cases were clearly detected and reconstructed with Tikhonov regularization. In Fig. 8 (c), the imaging accuracy was consistently improved after enhancement with U-Net, with an average ICC, RIE, and SSIM of 0.80, 0.59, and 0.92. Furthermore, by comparing images obtained with indenters of different sizes at the same location, it was possible to distinguish the size of the compressed regions based on the images. One exception is case 4, which exhibits a relatively low accuracy (the ICC and SSIM are only 0.65 and 0.88, and RIE is 0.75) even after U-Net enhancement. Additionally, the image could not be clearly distinguished from that of case 1, despite the difference in indenter diameters. Overall, the sensor developed in this study successfully fulfills the function of compressed region detection.

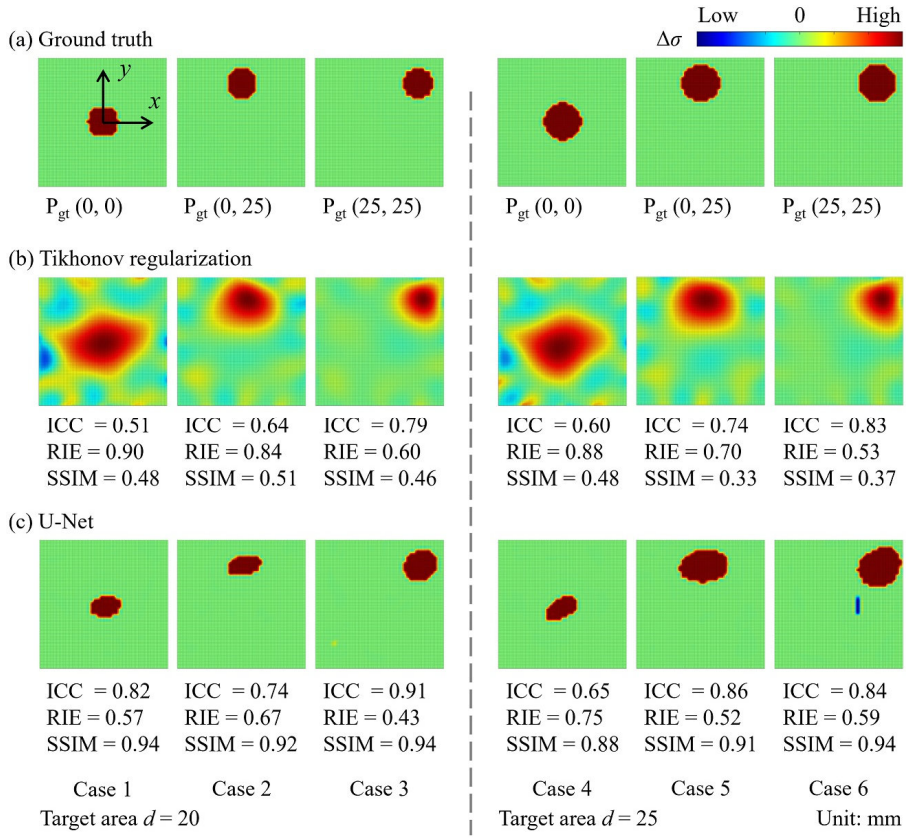

Fig. 8. Single compressed area tests. (a) ground truth of the setups, (b) the imaging results of Tikhonov regularization, and (c) the enhanced imaging results of U-Net, with an average ICC, RIE, and SSIM of 0.80, 0.59, and 0.92, respectively. In conclusion, the developed sensor is functional in tactile sensing.

Then, a positioning accuracy test was conducted with the 20 mm indenter. Because the sensor is symmetrical, nine points were selected within the first quadrant of the sensor coordinate, including the positive halves of the x-axis and y-axis. The tested positions were evenly distributed, with a distance of 12.5 mm between adjacent points along both the x-axis and y-axis. The centroid positions of the reconstructed images of targets are calculated to evaluate the positioning accuracy. Because the boundaries of the targets are not clear in the Tikhonov regularization imaging results, a threshold of 50 % of the peak value is set to distinguish between pixels inside and outside the targets.

As the test result shown in Fig. 9, the black solid dots represent the true position of the indenter, and the red crosses and green circles represent the reconstructed positions obtained using the Tikhonov regularization and the U-Net, respectively. The maximum, minimum, and average positioning errors of the Tikhonov regularization image are

3.75 mm, 1.12 mm, and 2.52 mm, respectively. After the enhancement of U-Net, the maximum, minimum, and average positioning errors were reduced to 3.44 mm, 0.92 mm, and 1.84 mm over a square with an edge length of 100 mm.

The multi-target tests were also conducted. As shown in Fig. 10, (a) represents the ground truth, (b) is the Tikhonov regularization images, and (c) is the U-Net enhanced images. Cases 7-10 are two-target tests, and cases 11 and 12 are three-target tests. From the figure, it can be observed that all targets were successfully detected. After enhancement with U-Net, the boundaries of the targets were clearly distinguished, although in the results of Tikhonov regularization, they are connected. In the two-target tests (Cases 7-10), the average ICC, RIE, and SSIM of the U-Net enhanced image are 0.85, 0.54, and 0.86, respectively. In the three-target tests (Cases 11 and 12), the corresponding values are 0.70, 0.78, and 0.70. Although the reconstruction accuracy decreases with an increasing number of targets, the developed sensor is still capable of detecting both single-target and multi-target compressed areas.

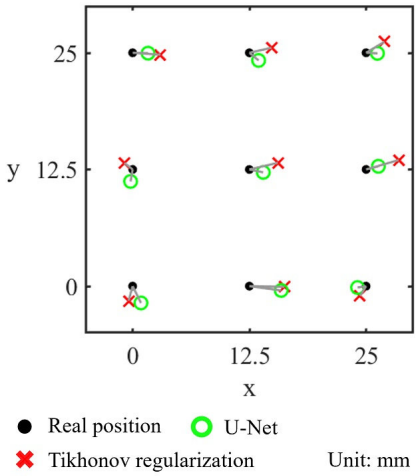

Fig. 9. Positioning accuracy test result, where 9 points are in the first quadrant of sensor coordinate are selected. The red crosses and green circles represent the reconstructed positions obtained using the Tikhonov regularization and the U-Net enhance images, respectively. After the enhancement of UNet, the maximum, minimum, and average positioning errors are 3.44 mm, 0.92 mm, and 1.84 mm over a square with an edge length of 100 mm.

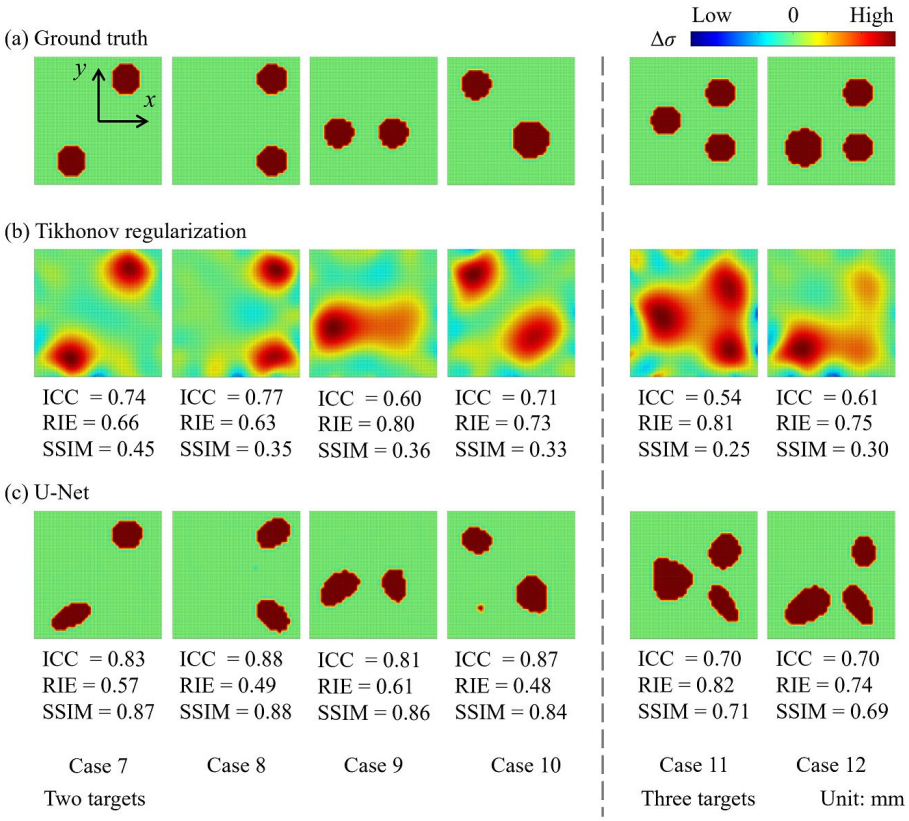

Fig. 10. Multi-target compression test. (a), (b) and (c) represent the ground truth, Tikhonov regularization images, and the U-Net enhanced images, respectively. Cases 7-10 are two-target tests, where the average ICC, RIE, and SSIM are 0.85, 0.54, and 0.86, respectively. Cases 11 and 12 are three-target tests, and the average ICC, RIE, and SSIM are 0.70, 0.78, and 0.70. All compressed areas are clearly detected.

D. Self-healing tests

The same experimental setup was used in self-healing experiments, as shown in Fig. 11. In this experiment, the performance of the sensor before damage is given as a reference, as shown in Fig. 11 (1). The 25 mm indenter head was used to manually apply pressure to the sensor. Because the pressure sensing performance is already validated with the test platform, manual pressing was adopted here to ensure a continuous experimental process from compressed area sensing to damage detection and discrimination to self-healing, achieving a clearer illustration of the functionalities of the proposed self-healing sensor. Cases 1 and 2 correspond to two compressed regions located in the first and third quadrants of the sensor coordinate system. For each case, (a), (b), and (c) represent the photographs, the measurement results obtained using Tikhonov regularization, and the results enhanced by U-Net, respectively. As shown, the compressed areas were clearly detected.

In the second step of Fig. 11 (2), a blade was used to cut a 20 mm length of damage in the first quadrant of the sensor (a zoomed-in photo is shown in the first image of Fig. 11 (3)). The imaging results, presented in case 3 of Fig. 11 (2), demonstrate that the sensor clearly detected the location and shape of the damage. Furthermore, in case 4, pressure was applied to the undamaged part of the sensor. The imaging results indicate that even partially damaged, the undamaged section of the sensor still functions normally in detecting compression, while also successfully detecting the damage.

Thirdly, the in-situ self-healing procedure was carried out, as shown in Fig. 11 (3). The heat pad was placed on the damaged area, and the silicone rubber pad was placed on top of the heat pad. The same as the self-healing composite test, the sensor was self-healing with a temperature of 90 ℃ for 2 hours, then cooled down at room temperature. One thing to note is that the heating temperature and duration must be carefully controlled. Otherwise, the self-healing composite sensing layer may adhere to the metal shortcut layer, leading to sensor failure. In such cases, it is necessary to wait until the sensor has completely healed and cooled, then gently pull and separate the sensing layer from the shortcut layer with tape or a suction cup to restore its functionality. The healed wound is shown in the rightmost image of Fig. 11 (3). It can be observed that the previously damaged region has healed, leaving only a faint scar (highlighted by the red dashed line box).

The sensor performance after self-healing is presented in Fig. 11 (4). Case 5 is the sensor after self-healing without compression, which can also be considered an assessment of the damage recovery. As shown in (b), the damaged area still with a faint blue color in the image, but is significantly lighter in color compared to cases 3 and 4. In (c), it is evident that the damaged area can no longer be detected by the U-Net. These results indicate that the composite has successfully carried out the self-healing process. However, the results also suggest that the composite does not achieve complete self-healing, which is consistent with the sample self-healing test in section “IV. A, Self-healing property of the composite”.

Additionally, in (b), several faint red “artifacts” can be observed in the image. This phenomenon can be explained by the results presented in section “IV. A, Self-healing property of the composite”. When the heat pad is used to trigger self-healing, the conductivity in the heated area decreases and gradually recovers over time, as shown in sample 1 in Fig. 5. However, the experiment also indicates that the conductivity does not fully return to its initial value, but rather remains higher. This leads to the appearance of such artifacts. Then, as seen in Cases 6 (b) and (c), when the damaged area is compressed after self-healing, it fails to correctly image the compressed region.

Before discussing how to address this issue and restore the sensor function, we first revisit the time-differential EIT used in this research. According to the theoretical principles outlined earlier in section 2, time-differential EIT requires acquiring a baseline voltage V_0 (the boundary voltage when no target is present within the sensor) as a reference. Then, after the target appears, a new voltage V_1 is acquired, and imaging is performed based on the difference between the two voltage data. In the previous imaging process, the baseline voltage V_0^{old} was obtained before the damage, but the composite cannot achieve complete restoration after self-healing, as shown in case 5, leading to a difference. Therefore, restoring the function of the sensor is simple, which is acquiring a new baseline voltage V_0 after self-healing.

The imaging results using the new baseline voltage V_0 with Tikhonov and U-Net are shown in (b’) and (c’), respectively. The compression-free imaging results are presented in cases 5 (b’) and (c’). It is evident that the artifacts have been significantly reduced. As shown in case 6 (b’) and (c’), the compressed test results illustrate that the previously damaged area has fully regained its tactile sensing capability after self-healing. Case 7 demonstrates that the undamaged areas retained functionality (with the updated V_0). These experimental results demonstrate that the proposed sensor successfully integrates tactile sensing, damage detection, and self-healing capabilities.

Furthermore, the performances of the self-healed area are evaluated in case 8, using the same experimental platform and process in section “IV. C, Tactile measurement tests”. To be consistent with the former test, the 20 mm indenter was used in this test. For positioning accuracy, the error e_{pos} in the self-healed area was 3.74 mm and 2.41 mm for Tikhonov and U-Net imaging, respectively. These values did not exceed the maximum errors of 3.75 mm for Tikhonov imaging and 3.44 mm for U-Net imaging before damage. Therefore, it can be considered that the positioning accuracy was fully restored after self-healing. For the image quality of the compressed area, the ICC, RIE, and SSIM of the U-Net enhanced image are 0.76, 0.65, and 0.92, respectively. Compared to the average ICC, RIE, and SSIM values of 0.80, 0.59, and 0.92 in the single-area tests shown in Fig. 8, and especially compared to case 3 (0.91, 0.43, 0.94 for ICC, RIE, and SSIM, respectively), which has the most similar setup, the ICC and

SSIM are higher, and the RIE is lower. Therefore, it is reasonable to consider that the image quality was affected by the damage and was not fully restored through the self-healing process, as well as by the conductivity changes induced by heating. Eliminating this influence will be a key focus of our future research.

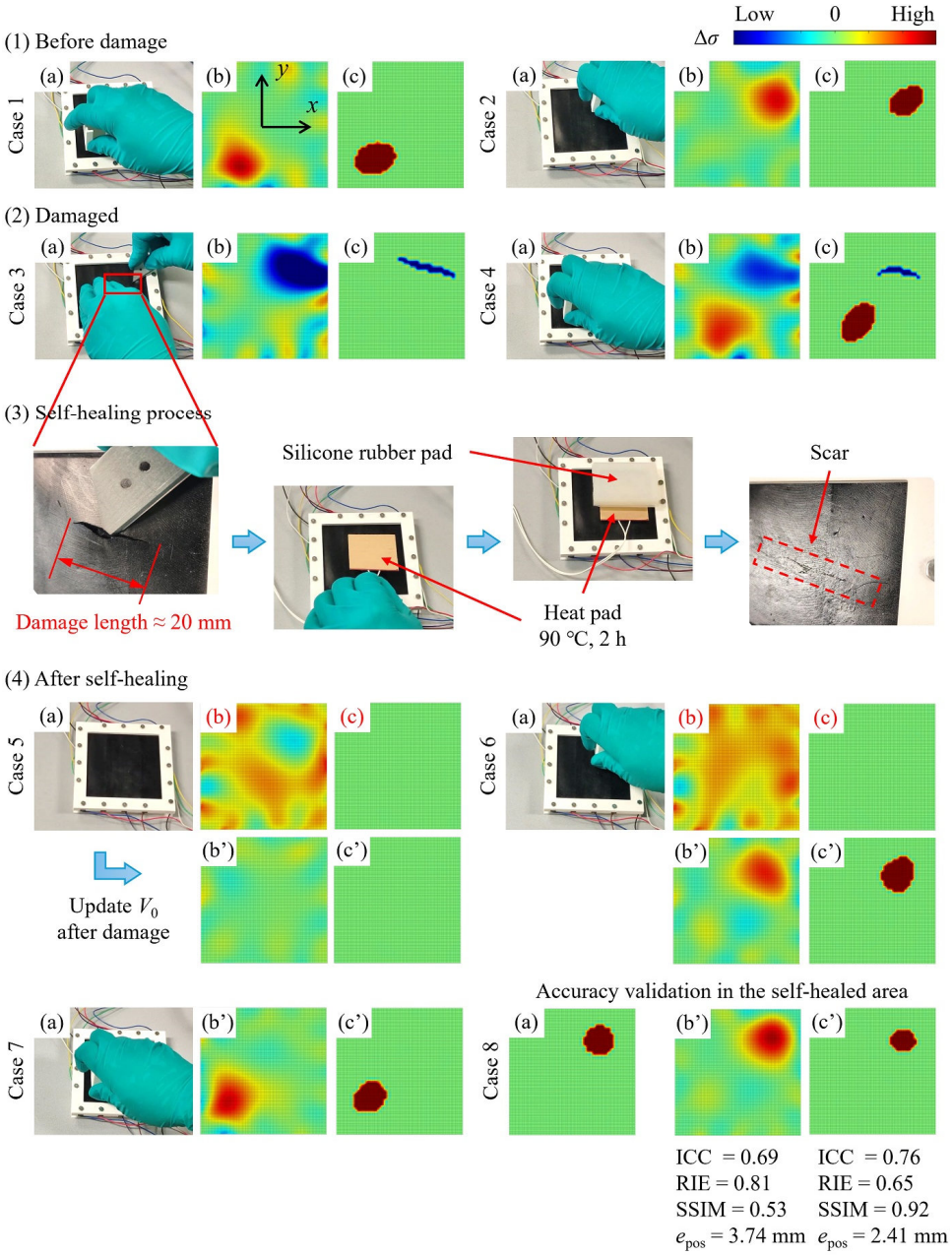

Fig. 11. Self-healing test. From (1) - (4) the sensor is at the stage of before damaged, damaged, in the self-healing process, and after self-healing. In each stage, (a), (b), and (c) represent the photographs, the measurement results obtained using Tikhonov regularization, and the results enhanced by U-Net. In (2), the sensor is able to detect the damaged area and also the compressed area, even if it is partially damaged. In (3), the sensor can achieve in-situ self-healing. In (4), (b) and (c) represent the imaging results using the baseline voltage V_0^{old} obtained before the damage, while (b') and (c') represent that after updating V_0. It is evident that after self-healing, simply reacquiring V_0 allows the sensor to fully regain its tactile sensing capability. Comparing the results of case 8 with the previous single-target tests in Fig. 8 and positioning test in Fig. 9, it can be observed that after damage and self-healing, the position accuracy was fully restored, while the result of ICC, RIE, and SSIM showed a slight accuracy decrease.

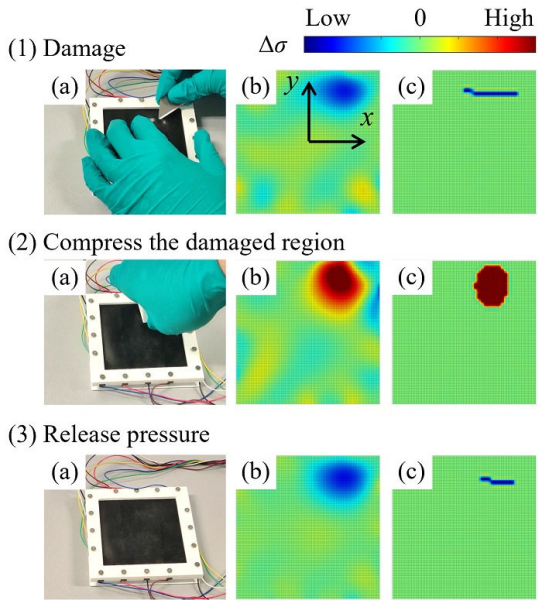

Fig. 12. A special case is considered where pressure is applied to a damaged region. A damaged region is introduced in (1), and in (2), pressure is applied to this region. The imaging result in (2) indicates that when the two regions overlap, the sensor displays a signal of compression. This occurs because, although the sensing layer in the damaged area is locally non-conductive, the applied pressure brings the non-conductive region into connected with the shortcut layer. In (3), once the pressure is released, the region is again identified as damaged.

We further investigate a specific scenario, that is, how the sensor responds when pressure is applied directly to a damaged region. The experimental results are presented in Fig. 12. It is observed that the sensor produces a pressure signal in this scenario. We attribute this phenomenon to the following mechanism, although the sensing layer becomes electrically disconnected in the damaged region, applied pressure brings the sensing layer into contact with the shortcut layer. This contact effectively bridges the disconnection, and furthermore, causes a high equivalent local conductivity, the same as compressing the undamaged region. Once the pressure is removed, the region reverts to appearing damaged.

Additionally, a comparison between Fig. 12 (3) (b) and case 4 (b) and case 5 (b) in Fig. 11 (4) reveals that no red artifacts appear in Fig. 12 (3) (b), even though this region is already damaged. This observation supports our previous hypothesis that such artifacts are not caused by the damage itself or residual low conductivity in an incompletely healed scar. Instead, they result from changes in composite conductivity introduced by the heating process during self-healing.

Future work will focus on a more detailed investigation of the relationship between temperature and conductivity in the self-healing composite, establishing the relationship among conductivity, temperature, and healing duration, and applying compensation strategies during the calculation of the Jacobian matrix in EIT imaging. These insights will be used to recalibrate the sensor after healing, reducing the impact of the self-healing process on sensing accuracy. Moreover, these findings also demonstrate that EIT is a potential approach for monitoring the healing state, by monitoring the thermal effects on the electrical properties during the self-healing process. We believe this can enable a more comprehensive and precise assessment of healing performance, and will also be investigated in our future works.

V. Conclusion

This study proposes a novel self-healing large-area tactile sensor with damage detection capabilities. The sensor achieves self-healing through the DA composite and enables tactile and damage detection based on EIT and a sandwich sensor structure design. In the proposed sensor, compression and damage cause completely opposite trends in conductivity changes, enabling truly selective detection of compression and damage without the need for complex algorithms.

To reconstruct images of tactile and damaged regions, a “two-step” AI-enhanced imaging method is employed. The sensor performance was first validated through single-target and multi-target measurements, as well as positioning accuracy tests. Then, damage and self-healing experiments are conducted on the sensor. The experimental results demonstrate that the sensor can clearly detect both tactile and damaged regions. Moreover, even when partially damaged, the undamaged sections retain their tactile sensing functionality. Furthermore, the sensor is capable of in-situ self-healing, eliminating the need for disassembly. After healing and a simple process of updating the baseline voltage of time differential EIT, the damaged area fully restores its original functionality.

On the other hand, we acknowledge that our work is still at an early stage, especially in terms of improving the sensing accuracy and addressing the slight reduction in accuracy observed after self-healing. To improve the accuracy of the sensor, we will investigate the optimization of the sensor, including electrode design and arrangement, and more advanced imaging algorithms. To reduce the accuracy loss, in future research, we will focus on enhancing the self-healing capability of the material, investigating the temperature-dependent characteristics of the conductivity of the composite, and improving the compensation algorithm.

Acknowledgements

Huaijin Chen is supported by China Scholarship Council (CSC) under NO. 202106830032.

Kevin Langlois and Seppe Terryn are supported by a personal grant from the Wetenschappelijk Onderzoek (FWO) under grant 1258523N and 1274125N.

Seyedreza Kashef Tabrizian acknowledges VUB research council for the postdoctoral grant OZR4307.

FWO SBO Sublime and the Flemish Government under the program Onderzoeksprogramma Artificiële Intelligentie (AI) Vlaanderen.

REFERENCES

[1] D. Silvera-Tawil, D. Rye, M. Soleimani, and M. Velonaki, "Electrical Impedance Tomography for Artificial Sensitive Robotic Skin: A Review," IEEE Sensors Journal, vol. 15, no. 4, pp. 2001-2016, 2015, doi: 10.1109/JSEN.2014.2375346.

[2] Z. Cui, Y. Yu, and H. Wang, "Recent Developments in Impedance-Based Tactile Sensors: A Review," IEEE Sensors Journal, vol. 24, no. 3, pp. 2350-2366, 2024, doi: 10.1109/JSEN.2023.3339791.

[3] J. Li and K. M. Lee, "A Novel Method for Soft Contact Sensing Based on Electrical Impedance Sensitivity Images," IEEE Sensors Journal, vol. 22, no. 10, pp. 9296-9305, 2022, doi: 10.1109/JSEN.2022.3163521.

[4] H. Lee, D. Kwon, H. Cho, I. Park, and J. Kim, "Soft Nanocomposite Based Multi-point, Multi-directional Strain Mapping Sensor Using Anisotropic Electrical Impedance Tomography," Scientific Reports, vol. 7, no. 1, p. 39837, 2017/01/25 2017, doi: 10.1038/srep39837.

[5] Y. J. Jeong, Y. E. Kim, K. J. Kim, E. J. Woo, and T. I. Oh, "Multilayered Fabric Pressure Sensor for Real-Time Piezo-Impedance Imaging of Pressure Distribution," IEEE Transactions on Instrumentation and Measurement, vol. 69, no. 2, pp. 565-572, 2020, doi: 10.1109/TIM.2019.2903701.

[6] H. Chen, X. Yang, J. Geng, G. Ma, and X. Wang, "A Skin-Like Hydrogel for Distributed Force Sensing Using an Electrical Impedance Tomography-Based Pseudo-Array Method," ACS Applied Electronic Materials, vol. 5, no. 3, pp. 1451-1460, 2023/03/28 2023, doi: 10.1021/acsaelm.2c01394.

[7] H. Zhang, A. Kalra, A. Lowe, Y. Yu, and G. Anand, "A Hydrogel-Based Electronic Skin for Touch Detection Using Electrical Impedance Tomography," Sensors, vol. 23, no. 3, doi: 10.3390/s23031571.

[8] K. Park, H. Yuk, M. Yang, J. Cho, H. Lee, and J. Kim, "A biomimetic elastomeric robot skin using electrical impedance and acoustic tomography for tactile sensing," Science Robotics, vol. 7, no. 67, p. eabm7187, 2022, doi: doi:10.1126/scirobotics.abm7187.

[9] H. Chen, Z. Wang, K. Langlois, T. Verstraten, and B. Vanderborght, "A Structure Modality Enhanced Multimodal Imaging Method for Electrical Impedance Tomography Pressure Distribution Measurement," IEEE Transactions on Instrumentation and Measurement, vol. 73, pp. 1-13, 2024, doi: 10.1109/TIM.2024.3436112.

[10] Z. Wang, H. Chen, K. Wang, B. Vanderborght, and S. Terryn, "A Variable Sensing Range Electrical Impedance Tomography Sensor for Robot Electric Skins," IEEE Robotics and Automation Letters, vol. 10, no. 3, pp. 2726-2733, 2025, doi: 10.1109/LRA.2025.3533964.

[11] H. Lee, K. Park, J. Kim, and K. J. Kuchenbecker, "Piezoresistive textile layer and distributed electrode structure for soft whole-body tactile skin," Smart Materials and Structures, vol. 30, no. 8, p. 085036, 2021/07/13 2021, doi: 10.1088/1361-665X/ac0c2e.

[12] S. Yoshimoto, Y. Kuroda, and O. Oshiro, "Tomographic Approach for Universal Tactile Imaging With Electromechanically Coupled Conductors," IEEE Transactions on Industrial Electronics, vol. 67, no. 1, pp. 627-636, 2020, doi: 10.1109/TIE.2018.2879296.

[13] H. Dong, X. Wu, D. Hu, Z. Liu, F. Giorgio-Serchi, and Y. Yang, "Learning-Enhanced Electronic Skin for Tactile Sensing on Deformable Surface Based on Electrical Impedance Tomography," IEEE Transactions on Instrumentation and Measurement, vol. 74, pp. 1-9, 2025, doi: 10.1109/TIM.2025.3546404.

[14] H. Dong, R. B. Liu, L. Micklem, S. P. E, F. Giorgio-Serchi, and Y. Yang, "Data-Efficient Tactile Sensing With Electrical Impedance Tomography," IEEE Sensors Journal, vol. 25, no. 11, pp. 19724-19733, 2025, doi: 10.1109/JSEN.2025.3557949.

[15] D. Silvera Tawil, D. Rye, and M. Velonaki, "Interpretation of the modality of touch on an artificial arm covered with an EIT-based sensitive skin," The International Journal of Robotics Research, vol. 31, no. 13, pp. 1627-1641, 2012/11/01 2012, doi: 10.1177/0278364912455441.

[16] D. Silvera-Tawil, D. Rye, and M. Velonaki, "Interpretation of Social Touch on an Artificial Arm Covered with an EIT-based Sensitive Skin," International Journal of Social Robotics, vol. 6, no. 4, pp. 489-505, 2014/11/01 2014, doi: 10.1007/s12369-013-0223-x.

[17] K. Park, H. Park, H. Lee, S. Park, and J. Kim, "An ERT-based Robotic Skin with Sparsely Distributed Electrodes: Structure, Fabrication, and DNN-based Signal Processing," in 2020 IEEE International Conference on Robotics and Automation (ICRA), 31 May-31 Aug. 2020 2020, pp. 1617-1624, doi: 10.1109/ICRA40945.2020.9197361.

[18] H. Park, W. Kim, S. Jeon, Y. Na, and J. Kim, "Graph-Structured Super-Resolution for Geometry- Generalized Tomographic Tactile Sensing: Application to Humanoid Faces," IEEE Transactions on Robotics, vol. 41, pp. 558-572, 2025, doi: 10.1109/TRO.2024.3508395.

[19] H. Chen, K. Langlois, J. Brancart, E. Roels, T. Verstraten, and B. Vanderborght, "A Novel Physical Human–Robot Interface With Pressure Distribution Measurement Based on Electrical Impedance Tomography," IEEE Sensors Journal, vol. 23, no. 18, pp. 21914-21923, 2023, doi: 10.1109/JSEN.2023.3303226.

[20] J. Kang, J. B. H. Tok, and Z. Bao, "Self-healing soft electronics," Nature Electronics, vol. 2, no. 4, pp. 144-150, 2019/04/01 2019, doi: 10.1038/s41928-019-0235-0.

[21] M. Qi et al., "Bioinspired Self-healing Soft Electronics," Advanced Functional Materials, vol. 33, no. 17, p. 2214479, 2023/04/01 2023, doi: https://doi.org/10.1002/adfm.202214479.

[22] S. Terryn, D. Hardman, T. G. Thuruthel, E. Roels, F. Sahraeeazartamar, and F. Iida, "Learning-Based Damage Recovery for Healable Soft Electronic Skins," Advanced Intelligent Systems, vol. 4, no. 12, p. 2200115, 2022/12/01 2022, doi: https://doi.org/10.1002/aisy.202200115.

[23] D. Hardman, T. G. Thuruthel, and F. Iida, "Tactile perception in hydrogel-based robotic skins using data-driven electrical impedance tomography," Materials Today Electronics, vol. 4, p. 100032, 2023/06/01/ 2023, doi: https://doi.org/10.1016/j.mtelec.2023.100032.

[24] F. Sahraeeazartamar et al., "Diels–Alder Network Blends as Self-Healing Encapsulants for Liquid Metal-Based Stretchable Electronics," ACS Applied Materials & Interfaces, vol. 16, no. 26, pp. 34192-34212, 2024/07/03 2024, doi: 10.1021/acsami.4c07129.

[25] F. Sahraeeazartamar et al., "Designing Flexible and Self-Healing Electronics Using Hybrid Carbon Black/Nanoclay Composites Based on Diels–Alder Dynamic Covalent Networks," Macromolecules, vol. 57, no. 2, pp. 539-553, 2024/01/23 2024, doi: 10.1021/acs.macromol.3c01904.

[26] S. K. Tabrizian et al., "Soft Self-Healing Damage Localization Sensor With Reduced Measuring Electrodes," IEEE Sensors Journal, vol. 25, no. 2, pp. 2381-2391, 2025, doi: 10.1109/JSEN.2024.3507737.

[27] S. Ren, K. Sun, C. Tan, and F. Dong, "A Two-Stage Deep Learning Method for Robust Shape Reconstruction With Electrical Impedance Tomography," IEEE Transactions on Instrumentation and Measurement, vol. 69, no. 7, pp. 4887-4897, 2020, doi: 10.1109/TIM.2019.2954722.

[28] H. Chen, X. Yang, P. Wang, J. Geng, G. Ma, and X. Wang, "A Large-Area Flexible Tactile Sensor for Multi-Touch and Force Detection Using Electrical Impedance Tomography," IEEE Sensors Journal, vol. 22, no. 7, pp. 7119-7129, 2022, doi: 10.1109/JSEN.2022.3155125.

[29] A. Adler et al., "GREIT: a unified approach to 2D linear EIT reconstruction of lung images," Physiological Measurement, vol. 30, no. 6, p. S35, 2009/06/02 2009, doi: 10.1088/0967-3334/30/6/S03.

[30] Y. Yang and J. Jia, "An Image Reconstruction Algorithm for Electrical Impedance Tomography Using Adaptive Group Sparsity Constraint," IEEE Transactions on Instrumentation and Measurement, vol. 66, no. 9, pp. 2295-2305, 2017, doi: 10.1109/TIM.2017.2701098.

[31] C. Tan, S. Lv, F. Dong, and M. Takei, "Image Reconstruction Based on Convolutional Neural Network for Electrical Resistance Tomography," IEEE Sensors Journal, vol. 19, no. 1, pp. 196-204, 2019, doi: 10.1109/JSEN.2018.2876411.

[32] Y. Li, Q. Zhu, and Z. Liu, "Deep Learning for Image Reconstruction in Electrical Tomography: A Review," IEEE Sensors Journal, vol. 25, no. 9, pp. 14522-14538, 2025, doi: 10.1109/JSEN.2025.3554696.

[33] M. Vauhkonen, D. Vadasz, P. A. Karjalainen, E. Somersalo, and J. P. Kaipio, "Tikhonov regularization and prior information in electrical impedance tomography," IEEE Transactions on Medical Imaging, vol. 17, no. 2, pp. 285-293, 1998, doi: 10.1109/42.700740.

[34] O. Ronneberger, P. Fischer, and T. Brox, "U-net: Convolutional networks for biomedical image segmentation," in Medical image computing and computer-assisted intervention–MICCAI 2015: 18th international conference, Munich, Germany, October 5-9, 2015, proceedings, part III 18, 2015: Springer, pp. 234-241.

[35] S. Terryn et al., "A review on self-healing polymers for soft robotics," Materials Today, vol. 47, pp. 187-205, 2021/07/01/ 2021, doi: https://doi.org/10.1016/j.mattod.2021.01.009.

[36] S. Russo, S. Nefti-Meziani, N. Carbonaro, and A. Tognetti, "A Quantitative Evaluation of Drive Pattern Selection for Optimizing EIT-

Based Stretchable Sensors," Sensors, vol. 17, no. 9, doi: 10.3390/s17091999.
[37] S. Anand, P. Jandial, and R. Nersisson, "A technical survey on hardware configurations for electrical impedance tomography systems," in 2021 Innovations in Power and Advanced Computing Technologies (i-PACT), 2021: IEEE, pp. 1-6.
[38] Z. Xu et al., "Development of a Portable Electrical Impedance Tomography System for Biomedical Applications," IEEE Sensors Journal, vol. 18, no. 19, pp. 8117-8124, 2018, doi: 10.1109/JSEN.2018.2864539.
[39] Y. Wu, D. Jiang, A. Bardill, R. Bayford, and A. Demosthenous, "A 122 fps, 1 MHz Bandwidth Multi-Frequency Wearable EIT Belt Featuring Novel Active Electrode Architecture for Neonatal Thorax Vital Sign Monitoring," IEEE Transactions on Biomedical Circuits and Systems, vol. 13, no. 5, pp. 927-937, 2019, doi: 10.1109/TBCAS.2019.2925713.
[40] S. Hong, J. Lee, J. Bae, and H. J. Yoo, "A 10.4 mW Electrical Impedance Tomography SoC for Portable Real-Time Lung Ventilation Monitoring System," IEEE Journal of Solid-State Circuits, vol. 50, no. 11, pp. 2501-2512, 2015, doi: 10.1109/JSSC.2015.2464705.
[41] Y. Yang and J. Jia, "A multi-frequency electrical impedance tomography system for real-time 2D and 3D imaging," Review of Scientific Instruments, vol. 88, no. 8, p. 085110, 2017, doi: 10.1063/1.4999359.
[42] X. Zhang et al., "V-Shaped Dense Denoising Convolutional Neural Network for Electrical Impedance Tomography," IEEE Transactions on Instrumentation and Measurement, vol. 71, pp. 1-14, 2022, doi: 10.1109/TIM.2022.3166177.
[43] Y. Wu et al., "Bayesian Image Reconstruction Using Weighted Laplace Prior for Lung Respiratory Monitoring With Electrical Impedance Tomography," IEEE Transactions on Instrumentation and Measurement, vol. 72, pp. 1-11, 2023, doi: 10.1109/TIM.2022.3220279.
[44] W. Zhou, A. C. Bovik, H. R. Sheikh, and E. P. Simoncelli, "Image quality assessment: from error visibility to structural similarity," IEEE Transactions on Image Processing, vol. 13, no. 4, pp. 600-612, 2004, doi: 10.1109/TIP.2003.819861.
[45] Z. Chen and Y. Yang, "Structure-Aware Dual-Branch Network for Electrical Impedance Tomography in Cell Culture Imaging," IEEE Transactions on Instrumentation and Measurement, vol. 70, pp. 1-9, 2021, doi: 10.1109/TIM.2021.3092524.

Huaijin Chen, received the B.E. and M.Sc. degree from Nanjing University of Aeronautics & Astronautics (NUAA), Nanjing, China, in 2018 and 2021 respectively. He is currently a Ph.D. student in Vrije Universiteit Brussel (VUB), Brussels, Belgium. His research interests are mainly about electrical impedance tomography pressure sensor.

Zhanwei Wang, received the BEng and MEng degrees in the Department of Mechanical Engineering at Northeastern University, China in 2017 and 2020 respectively. He is now a PhD student at Brubotics at the Vrije Universiteit Brussels and is affiliated with Imec. His research focuses on self-healing and soft robotics, including soft actuators, intelligent responsive structures, and soft matter simulations.

Fatemeh Sahraeeazartamar, started her PhD in 2020 at the Physical Chemistry and Polymer Science (FYSC) laboratory from Sustainable Materials engineering (SUME) Department at Vrije Universiteit Brussel (VUB). She obtained her bachelor's and master's degree in polymer engineering from Tehran Polytechnic (AUT). During her Master's, she studied self-healing composites and blends with optimized properties based on Diels-Alder chemistry with a focus on developing sustainable polymers suitable for deformation and damage sensing applications in Soft Robotics. By investigating these polymers offering opportunities for self-healing behavior she contributed to fabrication of more durable electronic devices such as self-healing stretchable sensors that can autonomously repair damage and maintain their functionality over time to not only enhances the reliability of devices but also extends their operational life, making them ideal for applications requiring flexibility, resilience, continuous performance, and sustainability.

Seyedreza Kashef Tabrizian, completed his master's degree at FUM in Iran focusing on bionic hands. In September 2020, he began his PhD at VUB, focusing on self-healing soft robots capable of healing without human assistance. Since September 2024, he has been conducting his postdoctoral at VUB funded by VUB research council. His research focuses on endowing robots with advanced, biologically inspired capabilities through the use of smart robotic materials.

Kevin Langlois, received the degree of Doctor of Engineering Sciences at the Vrije Universiteit Brussel (VUB), Brussels, Belgium in 2022. The focus of his research is on safe, comfortable, and efficient human-robot interactions. He is currently a post-doctoral researcher supported by the FWO and affiliated to imec. His research interests include sensors for physical human-robot interfaces and rehabilitation robotics.

Seppe Terryn, graduated with his MSc in 2014 at VUB. During his PhD, he combined smart materials and robotics, pioneering the multidisciplinary field of "self-healing soft robots." His primary expertise lies in designing multifunctional materials, including self-healing polymers, for advanced (re) processing and (de-)manufacturing, as well as for new embodied intelligence and sustainability principles in smart devices like (flexible) electronics and (soft) robotics. His research has earned his FWO PhD, Junior, and Senior postdoc grants. Since 2024, he has been an associate professor at VUB, leading PhDs and postdocs in projects like EU FET SHERO, MSCA ITN SMART, and EIC Transition SHINTO.

Bram Vanderborght, received his PhD from the Vrije Universiteit Brussel in 2007. He performed research at JRL lab in AIST, Tsukuba (Japan) and did his post-doc researcher at the Italian Institute of Technology. Since 2009 he is professor at the VUB. He had an ERC starting grant and is currently coordinating three EU projects on smart and self-healing materials for soft robots. His research interests are human-robot collaboration for applications for health and manufacturing like exoskeletons, prostheses, social robots, drones and cobots. He is affiliated to the Interuniversity Microelectronics Institute (imec), Belgium, as scientific collaborator.